Induced anisotropy of chiral carbon nanotubes under combined tension-twisting

3 AUTHORS:

Bruno Faria
Technical University of Lisbon
7 PUBLICATIONS   **38** CITATIONS

SEE PROFILE

N. Silvestre
Technical University of Lisbon
155 PUBLICATIONS   **1,629** CITATIONS

SEE PROFILE

Jose Nuno A Canongia Lopes
Technical University of Lisbon
179 PUBLICATIONS   **8,313** CITATIONS

SEE PROFILE

Induced anisotropy of chiral carbon nanotubes under combined tension-twisting

B. Faria [a], N. Silvestre [a,*], J.N. Canongia Lopes [b]

[a] *Dept. of Civil Engineering and Architecture, ICIST, Instituto Superior Técnico, Technical University of Lisbon, Av. Rovisco Pais, 1049-001 Lisboa, Portugal*
[b] *Chemical & Biological Eng. Dept., CQE, Instituto Superior Técnico, Technical University of Lisbon, Av. Rovisco Pais, 1049-001 Lisboa, Portugal*

ARTICLE INFO

ABSTRACT

The twist-induced anisotropic behavior of chiral carbon nanotubes (CNTs), namely the (6,3) CNT, under combined tension-twisting is presented and discussed in this paper. CNT chirality triggers anisotropic responses that depend predominantly on the direction of twisting. Both the level of axial tension and twist-induced anisotropy play a key role in the stiffness and strength of the chiral CNT. Molecular dynamics (MD) simulations of (6,3) chiral CNT under pure tension, pure twisting and combined tension-twisting are performed. The anisotropy induced by the twisting direction was shown to be remarkable: the shear modulus for direct twisting is 25% higher than that for inverse twisting whereas the buckling torque for inverse twisting is 40% higher than that for direct twisting. In the post-buckling regime, the ovalization of the CNT is higher for inverse twisting than for direct twisting and we show that ovalization leads to a decrease of post-buckling torsional stiffness. The post-buckling torsional stiffness for direct twisting was much higher than for inverse twisting. We show that the twist-induced anisotropic behavior of the chiral CNT is much more evident when it concerns stiffness than strength. For this chiral CNT under low twist-to-tension ratios, direct twisting has no impact on the failure strain (it equals the pure tensile failure strain) while inverse twisting has great influence on it (it is half the pure tensile strain). The magnitude of the twist-to-tension ratio also affects the post-buckling torsional stiffness of the chiral CNT: under combined tension-twisting, the post-failure structure of the CNT is more ductile for inverse twisting and more brittle for direct twisting. To the authors' best knowledge, this is the first time the anisotropic behavior of chiral CNT under combined tensile-twisting loads is studied.

© 2012 Elsevier Ltd. All rights reserved.

1. Introduction

Carbon nanotubes (CNTs) exhibit unique mechanical, thermal and electrical properties. Extensive study of these properties has been conducted on the past two decades, with impressive results (Wang et al., 2010). The potential applications of CNTs as basic elements in nano-devices such as nano-drive systems, nano-actuators and nano-oscillators have been widely investigated. For instance, the use of CNT as spring elements in torsional paddle oscillators or twisting bearings in nano-electric motors prompted research on their mechanical behavior under different directional loads. Actually, combinations of both tensile and twisting loads are expected to occur in these applications and the understanding of CNT mechanical response to combined tensile-twisting loading is crucial for the design and optimization of current and future CNT-based devices (Williams et al., 2002; Fennimore et al., 2003). Nevertheless, the great majority of published works focus on the CNT behavior under *pure loadings*, either *pure tension* or *pure twisting* (Dumitrica et al., 2006; Geng and Chang, 2006; Chang, 2007). The behavior of CNTs under

the simultaneous action of tension and twisting has been scarcely studied. Sun and Liu (2008) used a continuum mechanics model to investigate the buckling of multi-walled CNTs under combined torque, axial loading and radial pressure. Despite being useful in many situations, continuum mechanics models do not take into account the effect of interatomic dynamic forces, the influence of anisotropic lattices and the progressive failure of C–C bonds. Conversely, molecular dynamics simulations (MD) have the capability to consider all these nanoscale phenomena. Li et al. (2010) reported the results of MD simulations of SiC nanowires under combined tension-twisting, showing that both the tensile failure stress and buckling stress decrease under combined tension-twisting. Li (2010) used MD simulations to show that the stretchability of graphene nanoribbons can be considerably strengthened by a small twist angle, which can help the C–C bonds to undergo large nonlinear deformations. These two works focused on nanowires and nanoribbons under combined tension-twisting.

Regarding the MD simulations of CNTs under combined tension-twisting, few works have been published (Jeong et al., 2007a,b, 2008; Talukdar and Mitra, 2010). Using MD, Jeong et al. (2007a) have shown that the tensile strength of CNTs under combined tension-twisting (i) decreases linearly under increasing twist and (ii) increases by filling the CNTs with small molecular compounds. Jeong et al. (2007b) also mentioned that the failure strength of CNTs under tension-twisting significantly differs from the failure strength for pure tensile loading and also from the predictions of failure criteria for macroscale tubes. Faria et al. (2011) also found similar conclusions, but for CNTs under combined compression-twisting. Jeong et al. (2008) also confirmed that prestressing CNTs significantly changes their critical torsional moment and stiffness, a fact that is relevant for applications such as torsional oscillators because the torsional stiffness is directly associated with the torsional oscillation frequency. Talukdar and Mitra (2010) used MD of CNTs to investigate their behavior under axial loading and twist, both for perfect and imperfect lattices including Stone–Wales defects. However, all these works (Jeong et al., 2007a,b, 2008; Talukdar and Mitra, 2010) were dedicated to the study of *armchair* CNTs ($n, m = 0$). None of these works dealt with either *zig–zag* CNTs ($n, m = n$) or *chiral* CNTs (n, m). To the authors' knowledge, the present paper shows for the first time the mechanical behavior (strength and stiffness) of *chiral* CNTs under *simultaneous tension-twisting*. In order to achieve this goal, the chiral CNT is subjected to a few combinations of simultaneous stretching and twisting, using the MD code LAMMPS (Plimpton, 1995). The C–C interaction parameters are modeled by the latest version of the AIREBO potential proposed by Stuart et al. (2000) that is based on the well-known Brenneŕs second generation bond order potential. It is shown that the combined effect of (i) CNT chirality, (ii) twist direction and (iii) level of axial tension leads to relevant anisotropy, which governs the stiffness, strength and collapse of chiral CNTs. Finally, it is mentioned that well known anisotropic effects such as "axial tension-induced torsion" and "torsion-induced axial elongation" are implicitly taken into account by MD simulations but are not explicitly measured and studied in this paper.

2. Overview of molecular dynamics

The molecular dynamics (MD) simulations were performed using the Large Scale Atomic/Molecular Massively Parallel Simulator (LAMMPS) Plimpton, 1995. The Adaptive Intermolecular Reactive Empirical Bond Order Potential (AIREBO), included in the LAMMPS software package was used to model the inter-atomic forces present in the covalent binding of carbon in the CNT structure. The AIREBO potential is an improved version of Brenneŕs well-known second generation Reactive Empirical Bond Order Potential (REBO), but includes a Lenhard-Jones potential form to describe the Van-der-Waals long-range interactions ($E_{i,j}^{LJ}$) and a torsional term for the σ-bond torsion ($E_{k,i,j,l}^{Tors}$). The general form for the AIREBO potential is

$$E = \frac{1}{2} \sum_i \sum_{j \neq i} \left[E_{ij}^{REBO} + \sum_{k \neq i,j} \sum_{l \neq i,j,k} E_{k,i,j,l}^{Tors} + E_{i,j}^{LJ} \right] \tag{1}$$

A more detailed description of the AIREBO potential can be found in Jeong et al. (2007a).

For a given CNT with radius R and length L, both end sections are located at $x = \pm L/2$ (x is the CNT axis). For pure tension, incremental stretching displacements are imposed in opposite directions, $\Delta u = -0.025$ Å for atoms located at $x = -L/2$ and $\Delta u = +0.025$ Å for atoms at located $x = +L/2$. These imposed displacements stretch the CNT by $\Delta u = 0.050$ Å in each increment. For pure twisting, incremental twisting is imposed to the C atoms located in both end sections of the CNT. The incremental rotation about the x axis is $\Delta\phi = +0.5° = +\pi/360$ rad for the atoms located at $x = -L/2$ and $\Delta\phi = -0.5° = -\pi/360$ rad for the atoms located at $x = +L/2$. Both rotations twist the CNT by $\Delta\phi = 1.0° = \pi/180$ rad. For combined tension-twisting, both loadings are applied simultaneously. For a given combination, a twist-to-tension ratio $\Delta\phi/\Delta u$ must be defined, which means that the CNT twists $\Delta\phi/\Delta u$ radians (rad) for each Angstrom (Å) that it is stretched.

During the simulations the CNTs are allowed to relax, reaching a new equilibrium state while maintaining the prescribed stretching displacement and twisting rotation. All simulations were performed at a temperature of 300 K using the canonical NVT ensemble and Nosé-Hoover thermostat. The newtonian equations of motion were integrated using the velocity-Verlet algorithm. A timestep of 0.8 fs was used and all simulations comprised 10.000 timesteps. The configurational (or strain) energy V of the CNT calculated at the end of each simulation corresponds to the average value of the energy within the last 4.000 timesteps. 400 simulations (increments) were performed in each analysis.

In order to study the mechanical behavior of chiral CNTs under combined tension-twisting, we have considered the ($n = 6, m = 3$) CNT with radius $R = \frac{2.46}{\pi} \sqrt{n^2 + m^2 + nm} = 3.1$Å, chiral angle $\theta = \text{arctg}(\frac{\sqrt{3}m}{2n+m}) = 21.2°$ and length $L = 41.0$ Å. The CNT, depicted in Fig. 1, has an aspect ratio $L/D = 6.6$ and comprises 336 C-atoms. The MD results of chiral CNT under *combined tension-twisting* are presented in Section 5. Previously, and in order to clarify the differences between *pure* and *combined* behavior, it is essential to characterize the chiral CNT under *pure*
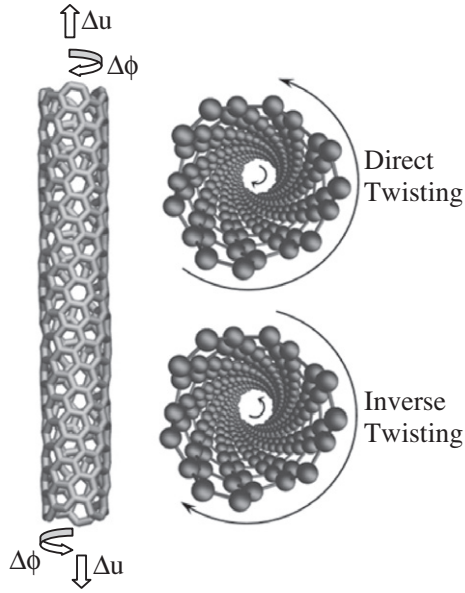
Fig. 1. (6,3) Chiral CNT under direct and inverse twisting rotations.

tension and *pure twisting*. These behaviors are presented in Sections 3 and 4, respectively.

3. Tensile behavior

The *pure tensile* behavior of (6,3) chiral CNT is discussed in this section. We have imposed incremental stretching displacements (Δu = 0.050 Å) and null twisting rotations ($\Delta \phi = 0$) to the CNT end-sections (boundary atoms). The results obtained from the MD simulations are shown in Fig. 2. Fig. 2(a) shows the variation of the strain energy per atom, V, as a function of axial strain, $\varepsilon = u/L$. Fig. 2(b) displays the variation of the force per atom, F, as a function of axial stretching, u (note that 1.0 eV/Å = 1.602 nN).

From Fig. 2(a), we can anticipate that the $V(\varepsilon)$ curve can be subdivided into four stages (I, II, III, IV). Using the LSM – Least Square Method, the $V(\varepsilon)$ curve in each of the stages I to III was fitted to the best polynomial regression that

maximizes the coefficient of correlation, ρ. The fitted expressions and ρ-values are

$$V_{\text{I}} = 20.7\varepsilon^2 + 0.15\varepsilon, \quad \rho^2 = 0.999 \tag{2}$$

$$V_{\text{II}} = -39.9\varepsilon^3 + 23.8\varepsilon^2 + 0.10\varepsilon, \quad \rho^2 = 0.999 \tag{3}$$

$$V_{\text{III}} = 9.6\varepsilon^2 + 1.37\varepsilon \quad , \rho^2 = 0.999 \tag{4}$$

According to Eqs. (2) and (4), energy varies quadratically with the strain in both stages I and III. However, the curvature of $V(\varepsilon)$ is higher in stage I than in stage III. Surprisingly, stage II (between stages I and III) is best characterized by a cubic dependence on the strain. Stage III ends with a maximum of energy that corresponds to a failure strain of ε_f = 0.275, which means that the CNT can be stretch up to 27.5% of its original length before failure occurs. Stage IV begins for strains higher than the failure strain ($\varepsilon > \varepsilon_f$) and is characterized by small drops in energy that suggest energy release caused by the breaking of C–C bonds, i.e., the CNT structural integrity starts to be compromised. Besides undergoing a sequential breaking of C–C bonds, the CNT also experiences a sequential rearrangement of C–C bonds, which also explains the large amount of small increases and small drops of $V(\varepsilon)$. As the elongation continues, a wire structure forms at the middle zone of the CNT (see Fig. 3(a)) and the complete rupture of the CNT is achieved at a later time. These four stages agree with those obtained by Mylvaganam and Zhang (2004) for MD simulations of (10, 10) armchair CNT and (17, 0) zig–zag CNT under pure tension. Later on, Agrawal et al. (2008) also analyzed the tensile behavior of (14, 14) armchair CNT and (24, 0) zig–zag CNT using MD simulations. The stress–strain curves obtained by Agrawal et al. (2008) also exhibit these four stages. Qualitatively similar constitutive relations have also been determined by other researchers worldwide (Geng and Chang, 2006), but mainly for zig–zag and armchair CNTs.

Fig. 2(b) represents the variation of force, F, with the axial displacement, u. Before CNT failure is achieved, the same three stages can be clearly seen. In each stage, the $F(u)$ curve was fitted by the best polynomial regression that maximizes the coefficient of correlation, ρ. These are
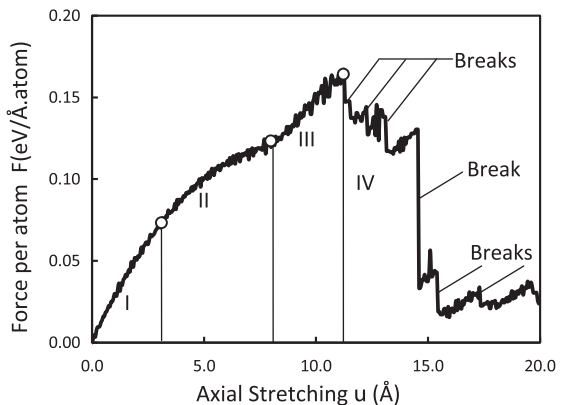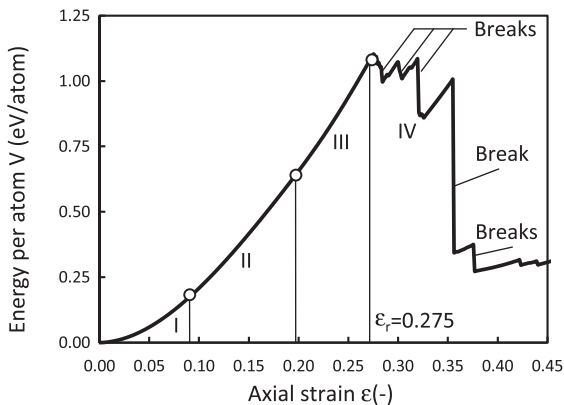

Fig. 2. (a) Variation of energy V with axial strain ε, and (b) Variation of force F with stretching u.
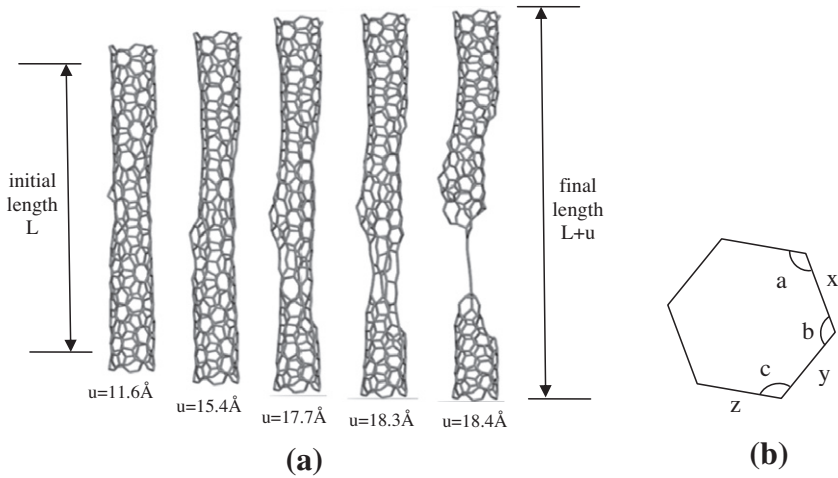
Fig. 3. (a) Deformed shapes of CNT in failure and post-failure (stage IV) and (b) labeling of bonds and angles.

$$F_{\mathrm{I}} = -0.023u, \quad \rho^2 = 0.997 \tag{5}$$

$$F_{\mathrm{II}} = -0.0015u^2 + 0.026u, \quad \rho^2 = 0.999 \tag{6}$$

$$F_{\mathrm{III}} = 0.014u, \quad \rho^2 = 0.994 \tag{7}$$

In accordance with the Eqs. (5) and (7), the force F varies linearly with the axial displacement u in stages I and III. It is seen that the slope of $F(u)$ is higher in stage I (initial stiffness $\partial F_{\mathrm{I}}/\partial u = 0.0234$ eV/Å^2 atom)∗ than in stage III (pre-failure stiffness $\partial F_{\mathrm{III}}/\partial u = 0.0137$ eV/Å^2 atom). In stage II, there is a quadratic variation of the force F with the displacement u. Finally, the maximum tensile force $F_f = 0.157$ eV/Å atom is reached at failure, corresponding to the displacement $u_f = 11.3$ Å. Stage IV (post-failure stage) is characterized by higher displacement values ($u > u_f$). In this stage, some C–C bonds break and localized regions of the CNT deteriorate. Fig. 3(a) shows a set of deformed shapes of the CNT in the stage IV.

Since force F is proportional to the first u-derivative of energy, we can say that Eqs. (2)–(7) are consistent: in stages I and III, the linear trends of $F(u)$ curve are directly related to the quadratic variation of the strain energy $V(\varepsilon)$. It is also clear that the initial stiffness ($\partial F_{\mathrm{I}}/\partial u = 0.0234$ eV/Å^2 atom) is not reached in the pre-rupture stage III ($\partial F_{\mathrm{III}}/\partial u = 0.0137$ eV/Å^2 atom), but only a fraction of it (58%). In the intermediary stage (stage II), the variation of $F_{\mathrm{II}}(u)$ is quadratic with negative curvature, which is consistent with the cubic variation of $V_{\mathrm{II}}(\varepsilon)$ Eq. (3), and there is a visible decrease of the curve slope, indicating that the stiffness $\partial F_{\mathrm{II}}/\partial u$ of the CNT decreases with axial displacement. The explanation for this evidence resides in the development of a subtle necking phenomenon in the middle zone of the CNT. This necking phenomenon is associated with a decrease of the CNT diameter. Fig. 4 depicts the evolution of the average diameter near the point of rupture with the imposed axial displacement. It is visible that the CNT diameter decreases linearly in stages I and III but remains almost unchanged in stage II. We can easily conclude that the linear decrease of diameter, which

is visible in stages I and III of Fig. 4(b), is associated with the preservation of a constant positive axial stiffness ($F_{\mathrm{I}}(u)$ and $F_{\mathrm{III}}(u)$ slopes). Additionally, the maintenance of the diameter in stage II (Fig. 4) is associated with a decrease of the axial stiffness ($F_{\mathrm{II}}(u)$ slope) as a softening behavior of the CNT takes place. From these results, it is not clear which parameters are responsible for the CNT diameter reduction and which relation exists between the stiffness and the diameter reduction. Fig. 4 also allow us to mention that the diameter reduction in chiral CNTs is lower than that observed in armchair CNTs but higher than the one evidenced by zig–zag CNTs (Faria et al., in press). Zig–zag CNTs have a higher circumferential stiffness and don't suffer diameter reduction. Conversely, armchair CNTs possess a lower circumferential stiffness and exhibit a high diameter reduction (Faria et al., in press).

From these data, it is also possible to evaluate the elastic properties and strength of the (6,3) chiral CNT. The Young's modulus $Y_{\mathrm{I}} = 0.78$ TPa was determined from the slope of the linear path in stage I, using $Y = \frac{\partial F_{\mathrm{I}}}{\partial u} \frac{L}{2\pi Rt}$, where t is the CNT thickness (we have considered $t = 3.4$ Å (Agrawal et al., 2008)). The obtained Y_{I} value agrees with the 0.77 and 0.82 TPa values obtained by Agrawal et al. (2006) and Talukdar and Mitra (2010), respectively, using MD simulations with a similar value of CNT thickness. Cooper and Young (2000) measured experimentally the Young's modulus of single-walled CNTs using Raman spectroscopy and obtained minimum values around 0.78 TPa, matching the Y_{I} value found in this study. Moreover, Leung et al. (2006) also found a value of $Y = 1.0$ TPa for chiral CNTs using $t = 2.58$ Å. Since Y is inversely proportional to the thickness t, the value $Y = 1.0$ TPa corresponds to $Y = 1.0$ TPa $\times \frac{2.58}{3.4} = 0.76$ TPa for a thickness $t = 3.4$ Å, which agrees with the result obtained in the present study. Additionally, the Young's modulus characterizing the elasticity of the CNT in pre-failure stage III was also determined from the slope of $F_{\mathrm{III}}(u)$, giving $Y_{\mathrm{III}} = 0.46$ TPa. It means that the stiffness of the CNT decreases about 40%. Finally, the CNT tensile strength $\sigma_t = 127$ GPa was determined from the maximum force F_f, using $\sigma_t = \frac{F_f}{2\pi Rt}$. This re-
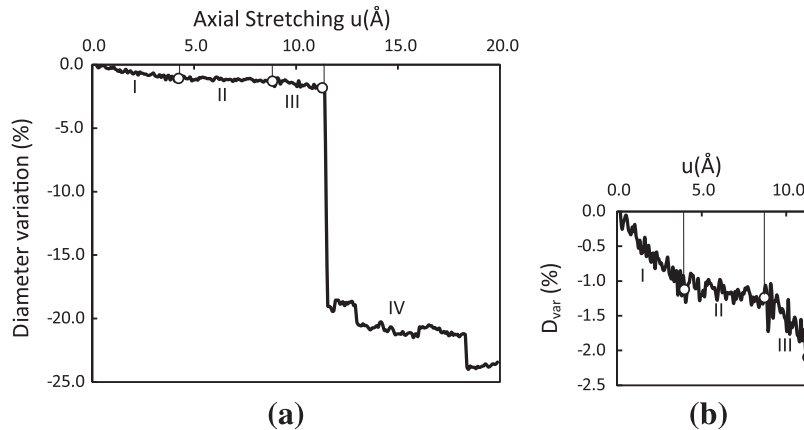
Fig. 4. (a) Variation of diameter (%) w.r.t axial stretching u(Å) and (b) amplified view of stages I–III.

sult agrees reasonably well with those obtained by Talukdar and Mitra (2010) and Jeng et al. (2004), who found tensile strengths between 100 and 158 GPa.

The failure of the chiral CNT and the hardening behavior experienced in stage III can be explained by taking into account the different distribution of forces in the C–C bonds. It is known (Wang et al., 2010) that the spatial orientation of the hexagon cells in the structure (i.e., its chirality) influences the response of the tensioned CNT and its failure strain. However, and for the specific case of chiral CNTs, explanations on this influence require a kinematic analysis of the C–C hexagon cells (i.e., the variation of bond lengths and angles with the imposed displacements). In the hexagonal lattice structure of the (6,3) CNT, the hexagonal cells are neither aligned with the CNT axis nor with the CNT perimeter due to the CNT chiral angle. Fig. 3(b) shows an hexagon cell of the (6,3) CNT, where x, y and z represent C–C bond directions and a, b and c represent the internal angles between adjacent C–C bonds. Fig. 5(a and b) show the variation of bond length with the imposed axial displacement for each of the three bonds (x, y, z – see Fig. 3(b)). From Fig. 5(a) it can be stated that there is always an increase in the bond length when a tensile load is imposed to the chiral CNT, regardless of the orientation of the bond. This length increase is somewhat proportional to the alignment of the bond with the CNT axis.

In order to explain this behavior, let us consider the x-, y- and z-bonds, which have "alignment angles" with respect to the CNT axis of 19.1°, 40.9° and 79.1°, respectively. Given its small "alignment angle", the x-bond is the one that is most aligned with the CNT axis. A small alignment angle promotes a better axial load transfer and induces the length of x-bond to increase more quickly than the others. This fact becomes evident from the observation of Fig. 5(a): the initial slope of the length variation of the x-bond is higher than the corresponding slopes in the y- or z-bond cases. The bond orientation is so influential to bond length shifts that, if we consider the axial stretching range between 0 and 8 Å (stages I and II), about 50% reduction in the alignment angle corresponds to doubling the bond length stretching rate. Thus, we conclude that the variation of bond length is approximately linear in stages I and II and that the initial slope of the x-bond length curve is approximately twice that of the initial slope of the y-bond length curve and four times that of the initial slope of the z-bond length curve. When the length of the x-bond reaches its critical length at around 8 Å of axial stretching (roughly 120% of the initial length), stage III begins to develop.
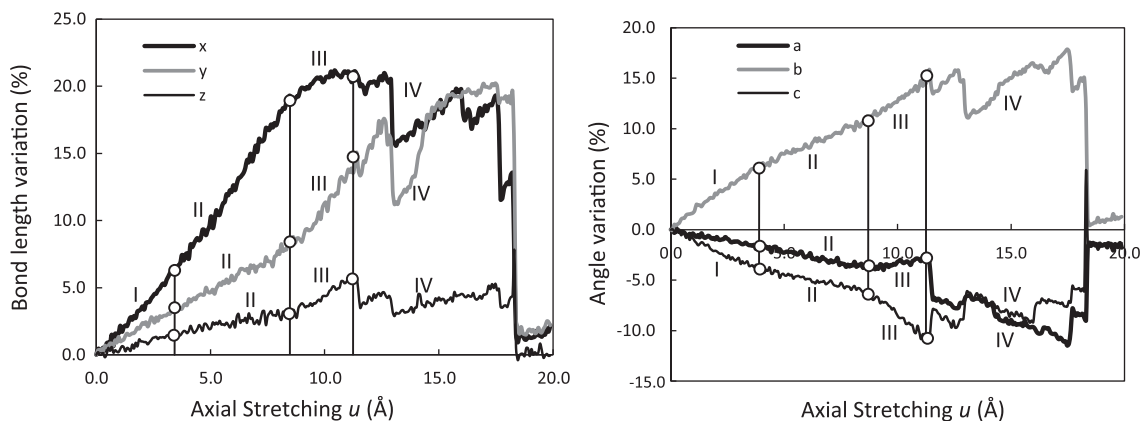

Fig. 5. Variation of (a) bond length (%) and (b) bond angle (%), with the axial stretching u(Å).

The necking phenomena, which had remained constant during stage II (from $u = 5$ to $u = 8$ Å), increases slightly during stage III (CNT diameter reduction of 2,5% – see Fig. 4). To understand this behavior we should pay attention to the variation of the c-angle. The beginning of stage III is characterized by a pronounced slowdown of the increase of the x-bond length, which means that the continuous axial stretching of the CNT is now assured by the enlargement of the y- and z-bonds, as it is visible in Fig. 5(a). How these bonds can increase their length if they have such marginal alignments with the CNT axis? The answer can be found by looking at the angle variation in Fig. 5(b): in stages I and II, the rates of increase of the b-angle and of the x-bond remain almost unchanged; this fact induces a smooth decrease of the a- and c-angles, and causes the y-bond to become more aligned with the CNT axis. As the y-bond becomes more aligned with the axial direction, it becomes possible (i) to transfer more force to the y-bonds and enlarge their length at a faster rate, and (ii) to relieve part of the strain in the x-bonds. Similarly, the z-bond length increases slightly due to a reduction in its alignment angle. In stage III, this type of strain transfer simultaneously decreases the c-angle. The closing of the c-angle is responsible for the slight diameter reduction observed in stage III (see Fig. 4). In fact, there is a close relation between c-angle variation (Fig. 4(b)) and diameter variation (Fig. 4) throughout all three stages, meaning that c-angle reduction is the main cause for diameter reduction. Eventually, the first x-bonds break somewhere in the middle zone of the CNTs. The location of the first bond that breaks is random due to small frequency oscillations of the CNT structure and localized tensions.

Rupture of the first x-bond implies the beginning of stage IV. This transition point coincides with the maximum of energy V (Fig. 2(a) and force F (Fig. 2(b)). The x-bonds do not break all at once, and so we don't see a huge and sudden drop in energy indicating a global and severe rupture of the CNT but only a set of repeated breaks of individual bonds – see the several deformed shapes in Fig. 3(a). The structural mesh of the CNT is irreversibly rearranged, C–C bonds are destroyed, new C–C bonds are created, and the characteristic hexagon cells are replaced by other geometric forms, leading to Stone–Wales defects in the hexagonal lattice. In order to react to axial loading without increasing its energy (Fig. 2(a)), the CNT diameter suddenly decreases (see Fig. 4) up to 20–25% as its length increases. Beyond this point, the variation of bond lengths and angles begin to scatter due to the forces that are released each time a bond breaks. Before total collapse, a wire structure forms in the middle of the CNT (see Fig. 3(a) – $u = 18.4$ Å). The explanation for this phenomenon lays on the mechanical asymmetric (anisotropy) that is exhibited by chiral CNTs, which is less evident in zig–zag and armchair CNTs (Faria et al., in press). It should be underlined that Marques et al. (2004) found experimental evidence of the wire structure formation in the middle of the CNT (see Fig. 3(a)), using a sequence of high-resolution TEM images detailing the reconstructive properties of carbon under tensile strain. It must also be stressed at this point that the emergence of these wire-like structure are an emergent phenomena caused by the use of sophisticated albeit empirical force-fields that try to capture in a simple manner the intricacies of carbon–carbon bonding in CNT and other carbon-based structures. This means that when the departures from the regular hexagonal lattices characteristic of CNTs become important[1] many of the results obtained must be tested against data obtained either by experiments or from first-principle (quantum-mechanics) methodologies. This clearly is out of the scope of the present work where the focus is to check where a widely used model will take us in terms of CNT properties when combinations of stretching and twisting constraints are imposed on the system. It must also be stressed that at the transition from stage III to stage IV the model is yielding reproducible and meaningful mechanical results and that, from a practical point of view, these are the working conditions which most of the applications in nanotechnology will be useful.

4. Twisting behavior

Pure twisting behavior of the (6,3) chiral CNT is discussed in this section. Now, we impose incremental twist rotations ($\Delta\phi = 0.01745 rad$) and null axial displacements ($\Delta u = 0$ Å) to the CNT ends. Because of the inherent chirality of the (6,3) CNT, both direct twisting and inverse twisting rotation increments had to be considered (see Fig. 1). Direct twisting corresponds to rotating both ends of the CNT in opposite directions following the rolling of the hexagonal lattice (top image in the right side of Fig. 1) while inverse twisting corresponds to rotating both CNT ends in opposite directions but opposing the rolling of the hexagonal lattice of the CNT (bottom image in the right side of Fig. 1).

Fig. 6(a) shows the variation of energy, V, with the angle of twist per unit of length, $\alpha = \phi/L$, for both inverse twisting (gray line) and direct twisting (black line). Unlike the tensile behavior, it is clear that large drops of energy do not occur for twisting behavior and only minor drops of energy take place for very large rotations. Generally speaking, the behavior of the chiral CNT under pure twisting exhibits four stages (I, II, III, IV) that can be clearly seen in Fig. 6(b). This Figure shows the variation of torque, T, with the twisting angle ϕ, and depicts two curves, one for inverse twisting (gray line) and the other for direct twisting (black line). In stages I and III, and using the LSM, the $V(\alpha)$ curves were fitted by polynomial regressions that maximize the correlation coefficient ρ. For direct twisting, the fitted curves are given by

$$V_{I} = 122.7\alpha^2 - 0.04\alpha, \quad \rho^2 = 0.999 \tag{8}$$

$$V_{III} = 33.0\alpha^2 + 2.74\alpha, \quad \rho^2 = 0.999 \tag{9}$$

while for inverse twisting, they read

$$V_{I} = 93.6\alpha^2 + 0.19\alpha, \quad \rho^2 = 0.999 \tag{10}$$

$$V_{III} = 17.7\alpha^2 + 3.41\alpha, \quad \rho^2 = 0.999 \tag{11}$$

---

[1] Stone-Wales defects are an initial consequence of such departures; wire-like features are a much more extreme outcome.
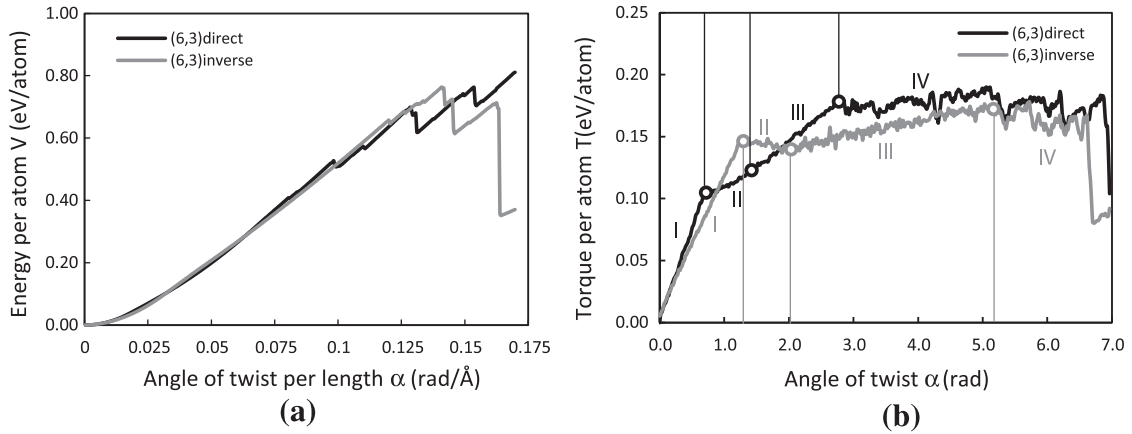
Fig. 6. Pure twisting: (a) variation of energy V with α and (b) variation of torque T with ϕ.

The $V(\alpha)$ curve in stage II was not fitted because it is too limited and corresponds to a transition stage between I and III. According to the four previous equations, the energy V varies quadratically with α in both stages I and III. However, the curvature of $V(\alpha)$ is much higher in stage I than in stage III. In stage IV, a few C–C bonds start to break and minor drops of energy take place. The directly twisted CNT is the first to undergo failure, about $\alpha_f = 0.080$ rad/Å ($\phi_f = 3.30$ rad). The inversely twisted CNT undergoes failure at about $\alpha_f = 0.12$ rad/Å ($\phi_f = 4.92$ rad).

A better understanding of this process is achieved by looking at Fig. 6(b). It is interesting to note that black and grey curves move away from each other right from the beginning (unstressed state), and even in linear stage I, their slope is slightly different. For inverse twisting (gray line in Fig. 6(b)), the four stages are characterized by:

- Stage I: T increases linearly with ϕ and reaches a maximum $T = 0.146$ eV/atom for $\phi = 1.34$ rad.
- Stage II: T decreases slowly with ϕ and reaches a minimum $T = 0.139$ eV/atom for $\phi = 2.04$ rad.
- Stage III: T increases slowly with ϕ and reaches a maximum $T = 0.178$ eV/atom for $\phi = 5.10$ rad.
- Stage IV: T varies randomly with ϕ, showing several drops.

For direct twisting (black line) there are also four stages, but with a slightly distinct trend:

- Stage I: T increases linearly with ϕ at a higher rate than for inverse twisting and reaches $T = 0.105$ eV/atom for $\phi = 0.84$ rad, which is lower than the maximum of inverse twisting.
- Stage II: T increases slowly with ϕ for $0.84 < \phi < 1.22$ rad.
- Stage III: T increases linearly with ϕ and reaches a maximum $T = 0.178$ eV/atom for $\phi = 2.84$ rad.
- Stage IV: T displays some scatter (rises and drops) and a maximum $T = 0.190$ eV/atom.

Similar trends were found by Khoei et al. (2011), but no definition of stages was made. In stages I and III, the $T(\phi)$

curves were also fitted by the best polynomial regression using the LSM. For direct twisting, the fitted curves are

$$T_I = 0.15\phi, \quad \rho^2 = 0.996 \tag{12}$$

$$T_{III} = 0.042\phi + 0.063, \quad \rho^2 = 0.997 \tag{13}$$

while for inverse twisting, they read

$$T_I = 0.12\phi, \quad \rho^2 = 0.991 \tag{14}$$

$$T_{III} = 0.011\phi + 0.118, \quad \rho^2 = 0.975 \tag{15}$$

For the fitted $T(\phi)$ curves Eqs. (12)–(15) in stages I and III, the torque varies linearly with the angle of twist. However, the slope of T_I is clearly higher than the slope of T_{III}.

First, let us look at stage I. In order to compare and validate the results, we have extracted the shear modulus of the (6,3) chiral CNT under twisting. The CNT shear modulus was determined from the slope of the $T_I(\phi)$ curves, using Eqs. (12) and (14)) and the definition $G = \frac{\partial T}{\partial \phi} \frac{L}{J_c}$, where the torsion constant of the circular section is $J_c = 2\pi R^3 t + \frac{\pi}{2} R t^3$. Note that for thin-walled CNTs ($t \ll R$), one has $J_c \cong 2\pi R^3 t$. Since R and t have similar magnitude for the (6,3) chiral CNT, the second term in J_c cannot be neglected. The computed CNT shear modulus is different for direct twisting ($G_d = 0.40$ TPa) and inverse twisting ($G_i = 0.32$ TPa). These results fall inside the range 0.41 ± 0.36 TPa determined experimentally by Hall et al. (2006) and are fairly close to 0.39 and 0.46 TPa, which are values obtained by Khoei et al. (2011) and Lu (1997), respectively. At the end of stage I, the CNT buckles into a helix shape with oval section having major width $2a$ and minor width $2b$ (see Fig. 7). The buckling torque for inverse twisting ($T_b = 0.146$ eV/atom) is much higher than the buckling torque for direct twisting ($T_b = 0.105$ eV/atom). Silvestre (Silvestre, 2012) proposed simple analytical formulas to estimate the buckling torque T_b of CNTs.

In stage II (transition state), the aspect ratio a/b of the oval section remains unaltered and the CNT continues to twist without excessive forces between C atoms. The slope of the $T(\phi)$ curve in stage II (see Fig. 6(b)) is slightly negative for inverse twisting and sharply positive for direct
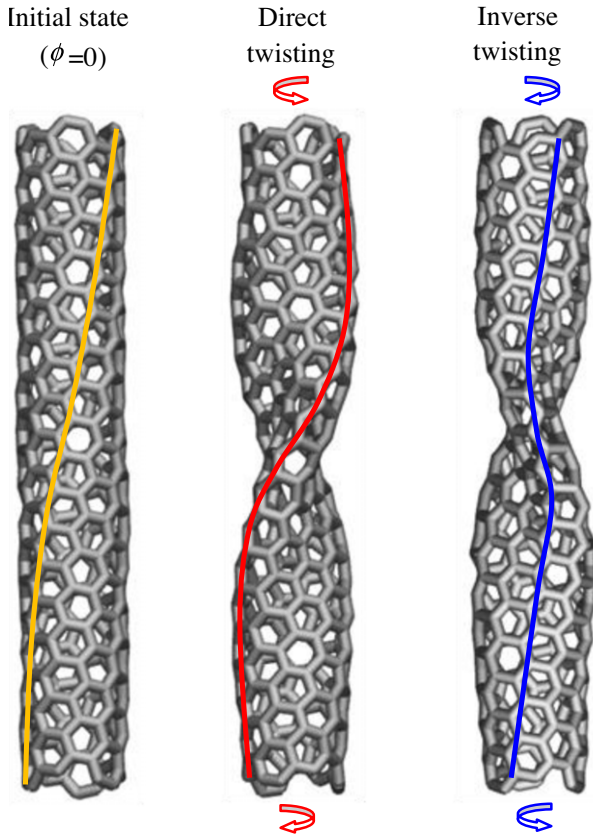
Fig. 7. Buckling modes of (6,3) chiral CNT under direct and inverse twisting (yellow line denotes the orientation of the zig–zag line that spirals around the CNT in the initial state; red and blue lines denote the deformed configuration of the zig–zag line in the CNT buckling mode under direct and inverse twisting, respectively).

twisting. When inverse twisting is applied to the chiral CNT, its lattice hexagonal structure twists around the tube axis so that it unrolls and softens (see Fig. 7): the yellow line denotes the zig–zag line that spirals around the CNT in the initial (unstressed) state and the blue line represents its deformed shape when the CNT buckles under inverse twisting. Note that the blue line tends to be parallel with the CNT axis and the lattice hexagonal softens. In stage II, this movement is possible for slightly negative torsional stiffness (softening), i.e., the twist evolves with small decrease of torque. After passing through the "zig–zag configuration" (blue line vertical), at the minimum $T = 0.140$ eV/ atom ($\phi = 2.04$ rad), the torsional stiffness of the inversely twisted CNT becomes positive again. Conversely, when direct twisting is applied to the chiral CNT, its lattice hexagonal structure twists around the CNT axis so that it rolls the helix even further (see Fig. 7): the red line represents the deformed shape of the yellow line when the CNT buckles under direct twisting. This motion increases torque, which means that torsional stiffness is now positive for direct twisting. Unlike inverse twisting, the softening behavior does not take place for direct twisting. Thus, it is clear that direct twisting bonds reach the maximum length sooner, because they have been stretched all along. This

is a comprehensible effect that shows the anisotropic behavior of chiral CNTs under twisting.

In stage III, the torque T evolves linearly with the twist ϕ, as it is seen from Eqs. (13) and (15). For direct twisting, the oval major width and the oval minor width obtained from the MD data are $2a = 7.4 \pm 0.3$ Å and $2b = 4.8 \pm 0.2$ Å, respectively. For inverse twisting, the oval major and minor widths are $2a = 8.5 \pm 0.4$ Å and $2b = 3.1 \pm 0.3$ Å, respectively. Thus, the chiral CNT becomes more ovalized for inverse twisting than for direct twisting. This relevant conclusion agrees with the fact that the slope of the $T_{III}(\phi)$ is higher for direct twisting Eq. (13) than for inverse twisting Eq. (15). This evidence raises the following question: is there any relation between the ovalization level and the torsional stiffness of the chiral CNT? The answer to this question can be found in the classical theory of torsion. From the mechanical point of view, the torsional stiffness of a hollow thin-walled section is given by the well-known Bredt's formula

$$J = \frac{4A^2 t}{P} \qquad (16)$$

where A is the area enclosed by the section mid-line and P is the section mid-line perimeter. However, this formula is valid only for thin-walled sections ($t/R \ll 1$), which is not the case of the present (6,3) chiral CNT, in which t and R are similar. Thus, we have to use the formula for the torsion constant of an oval (elliptic) solid section,

$$J = \frac{\pi a^3 b^3}{a^2 + b^2} \qquad (17)$$

where a and b are the major and minor semi-axis of the elliptic. For an elliptical hollow section, we have to apply

$$
\begin{aligned}
J &= J_{ext} - J_{int} \\
&= \frac{\pi (a + t/2)^3 (b + t/2)^3}{(a + t/2)^2 + (b + t/2)^2} - \frac{\pi (a - t/2)^3 (b - t/2)^3}{(a - t/2)^2 + (b - t/2)^2}
\end{aligned} \qquad (18)
$$

where J_{ext} and J_{int} are the torsional constants of the outside elliptic and inside elliptic, respectively. The MD data have shown that the perimeter of the CNT oval section remains almost unaltered. From the mechanical viewpoint, the state of pure shear in a hollow section bar does not alter its perimeter. Thus, we can assume that the perimeter of the oval (elliptic) remains that of the circular section $P = 2\pi R$. As ovalization progresses, the oval major semi-axis a increases for values above R while the oval minor semi-axis b decreases for values below R, and the oval aspect ratio a/b increases. With $P = 2\pi R = 19.5$ Å fixed, Fig. 8(a) shows the oval shapes for several values of the aspect ratio a/b. Fig. 8(b) shows the variation of ovalized-to-circular torsion constant ratio (J/J_c) with a/b. Note that $a/b = 1$ corresponds to the circular section ($J = J_c$). It is very interesting to note that the J/J_c ratio decreases with increasing a/b, meaning that the torsion constant of the oval section decreases as ovalization progresses. For small ovalization ratio ($a/b < 1.30$), the oval section torsional stiffness J is close to that of the circular section J_c. However, from moderate to high ovalization ratio ($1.30 < a/b < 4.6$), the drop of oval torsional stiffness is noticeable. Using
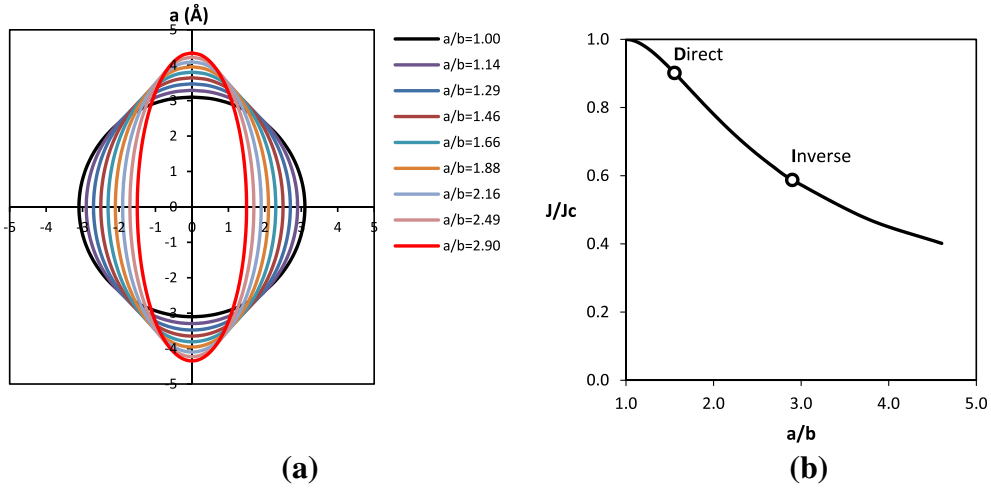
Fig. 8. (a) Circular and oval shapes for several aspect ratio a/b and (b) Variation of J/J_c with a/b (assumption of unaltered perimeter).

the a and b values measured from MD, the oval aspect ratio is $a/b = 7.4/4.8 = 1.54$ for direct twisting and $a/b = 8.5/3.1 = 2.74$ for inverse twisting. For $a/b = 1.54$ (direct twisting) and $a/b = 2.74$ (inverse twisting), the oval section torsional stiffness is 90% and 59% of the corresponding circular section value. Note also that the reduction of slope from stage I (T_I/ϕ) to stage III (T_{III}/ϕ) is not equal to the decrease of J/J_c from 100% to 90% and 59%, mainly due to the non-linear effects associated with the CNT helix shape. However, this analysis clearly shows that the twisting direction definitely influences the level of ovalization of the CNT and that this fact has a remarkable influence on its torsional stiffness. Furthermore, very recent and interesting investigation carried out by Lu et al. (2011) has shown that the radial deformation (i.e., ovalization) of a CNT plays a significant role in affecting its mechanical behaviour. They also found that single-walled CNTs with radius larger than 10.5 Å are prone to collapse under radial deformations.

Stage IV begins when the helix shape stops rotating about the CNT axis and the strains in C–C bonds begin to rise markedly due to excessive twisting. In stage IV, rupture of C–C bonds occurs when they exceed their maximum length and small drops are seen in the $T(\phi)$ curve for very large values of twist ϕ (Fig. 6(b)). Unlike the CNT tensile behavior, the twisted CNT does not separate apart completely but suffers bond rupture with rearrangements in the hexagonal lattice (formation of new bonds). These new bonds destroy locally the hexagonal lattice and introduce Stone–Wales defects in it, thus allowing stress release (which is clearly seen in the form of small drops in the energy curve). To some extent, this process allows further twisting with energy increase and without global rupture. Despite the distinct behavior of the chiral CNT under direct and inverse twisting, Fig. 6(b) shows that they fail for similar angles of twist: $\phi = 6.86$ rad $= 393°$ (direct twisting) and $\phi = 6.62$ rad $= 379°$ (inverse twisting). The CNT shear strength was determined from the maximum torque T_{max}, using $\tau = \frac{T_{max}R}{J_c}$. The computed CNT shear strength is slightly different for direct twisting ($\tau_d = 38.3$ GPa) and inverse

twisting ($\tau_i = 36.0$ GPa). These results agree with the shear strength $\tau = 33.6$ GPa obtained by Talukdar and Mitra (2010). Finally, it should be highlighted that the anisotropic behavior of the chiral CNT under twisting is much more evident for its stiffness ($(G_d-G_i)/(G_d + G_i)/2 = 0.055$) than for its strength ($(\tau_d - \tau_i)/(\tau_d + \tau_i)/2 = 0.015$).

5. Combined tension-twisting behavior

Pure tensile and pure twisting behaviors have been discussed in the previous sections. In this section we present and discuss a detailed study on the behavior of (6,3) chiral CNTs under combined tension-twisting. In order to evaluate the CNT behavior under different combinations of tension and twisting, the following two combinations (Δu vs $\Delta \phi$) are adopted,

$$\text{Combination A}: \quad \Delta u = 0.03536 \text{ Å}, \quad \Delta \phi = 0.01234 \text{ rad} \tag{19}$$

$$\text{Combination B}: \quad \Delta u = 0.02500 \text{ Å}, \quad \Delta \phi = 0.01511 \text{ rad} \tag{20}$$

For combination A, the twist-to-tension ratio $\Delta\phi/\Delta u = 0.349$ rad/Å is low, which means that the CNT twists 0.349 rad for each Å that it is stretched. For combination B, the twist-to-tension ratio $\Delta\phi/\Delta u = 0.605$ rad/Å is high, which means that the CNT twists 0.605 rad for each Å that it is stretched. Fig. 9 shows a set of four snapshots of the CNT under several twist-to-tension ratios: pure tension (1st snapshot), combination A (2nd snapshot), combination B (3rd snapshot), pure twisting (4th snapshot). The videos attached as Supplementary Information show the evolution of deformation of the CNTs under inverse and direct twisting. Fig. 9(a) presents the initial (unloaded) configuration of the CNT while Fig. 9(b–e) present the deformed shapes of the CNTs after 100, 200, 300 and 400 increment, respectively. The Figures in the left side ($9(b_1)$, $9(c_1)$, $9(d_1)$, $9(e_1)$) involve direct twisting of the
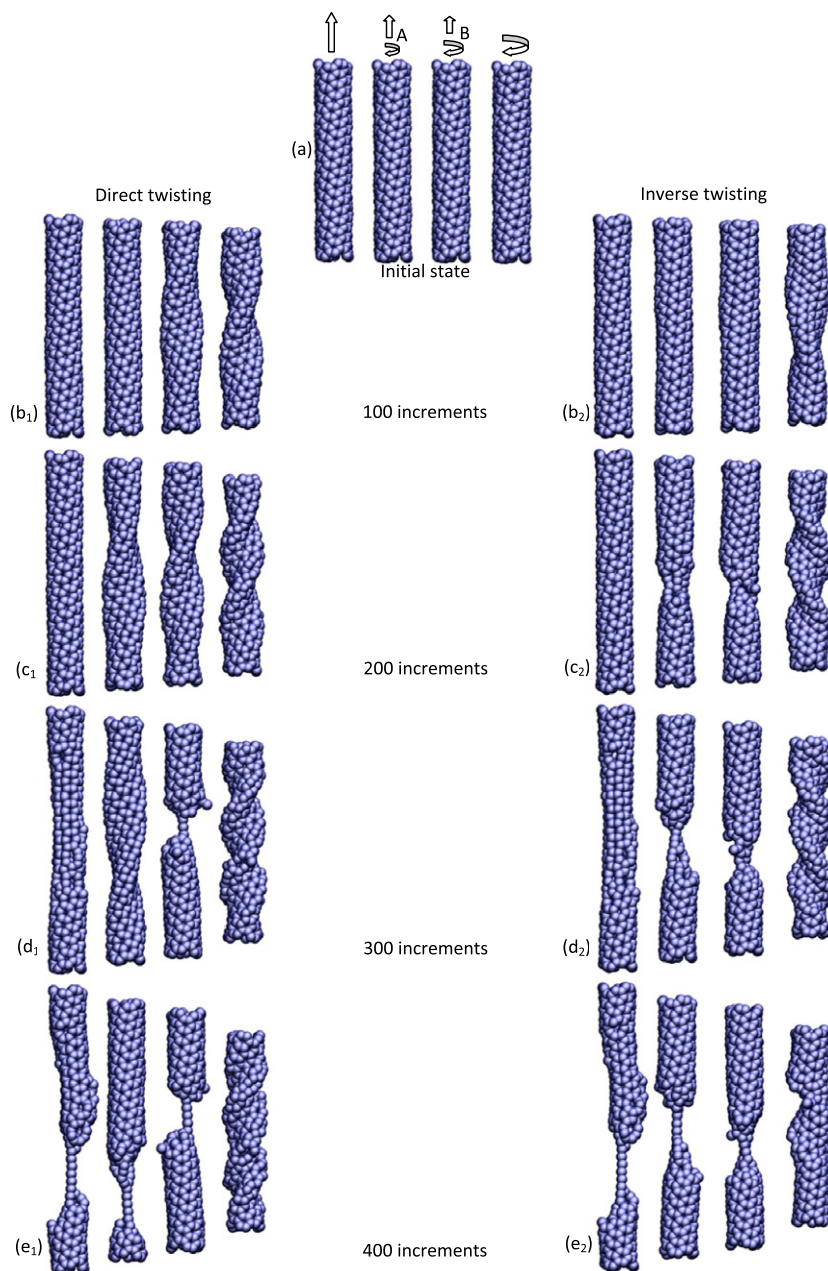
Fig. 9. Deformed shapes of the CNT under tension-to-twist rates: (a) initial (unloaded), (b) after 100 increments, (c) after 200 increments, (d) after 300 increments and (e) final (after 400 increments) - (b_1), (c_1), (d_1), (e_1) for direct twisting and (b_2), (c_2), (d_2), (e_2) for inverse twisting.

CNT while the Figures in the right side (9(b_2), 9(c_2), 9(d_2), 9(e_2)) involve inverse twisting of the CNT. From these Figures, it is observed that the CNT degradation and the evolution of its collapse is totally different if the CNT is under direct or inverse twisting. For combinations A (0.349 rad/Å – 2nd snapshot) and B (0.605 rad/Å – 3rd snapshot), the CNT also behaves differently for direct and inverse twisting – for instance, see the 2nd snapshot in Fig. 9(d_1) and (d_2). The tensioned CNT under direct twisting (combination A) tends to buckle into an helix-shape at early stages (200 increments – Fig. 9(c_1)) without rupture. A clear rupture

is visible only at 400 increments (Fig. 9(e_1)). The tensioned CNT under inverse twisting (combination A) does not tend to buckle into an helix-shape and shows a localized rupture at an early stage (200 increments – Fig. 9(c_2)). For combination B, a similar behavior is observed, but the CNT collapse occurs earlier for both direct and inverse twisting.

Figs. 10(a) and 11(a) display the variation of energy V with the axial strain, ε, for combinations A and B, respectively. Figs. 10(b) and 11(b) show the variation of the axial force, F, with the axial stretching, u, for combinations A and
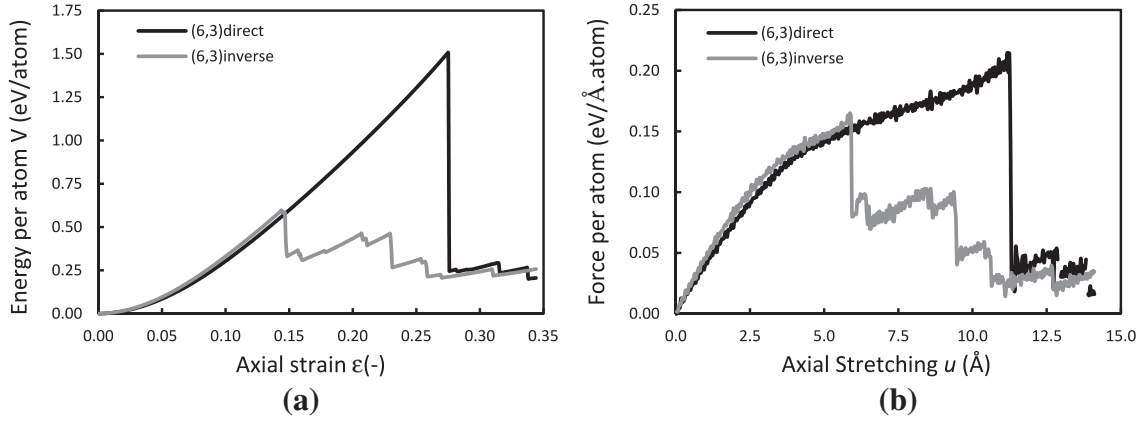
Fig. 10. Combination A: (a) variation of energy V with ε and (b) variation of force F with u.
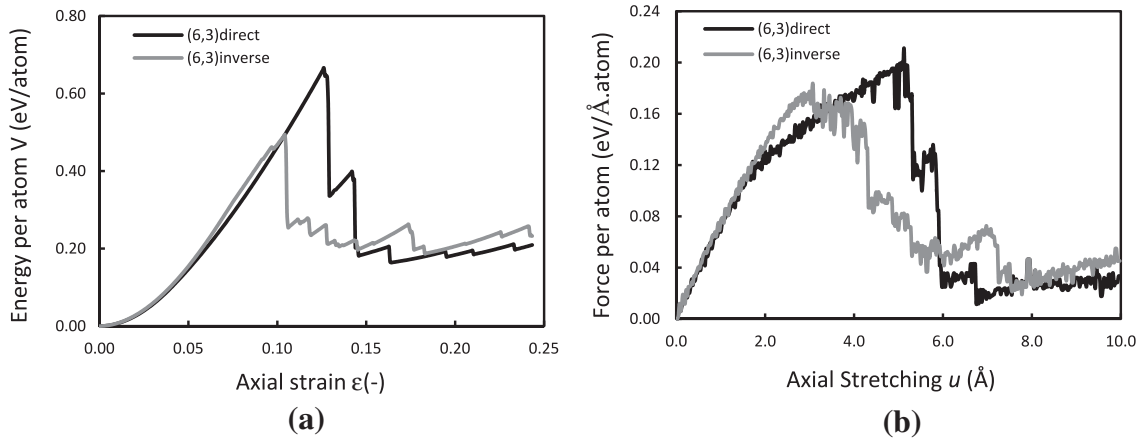

Fig. 11. Combination B: (a) variation of energy V with ε and (b) variation of force F with u.

B, respectively. In each Figure, black and gray lines correspond to the CNT under direct and inverse twisting, respectively. The observation of these Figures enable the following relevant remarks:

- From the comparison between Figs. 10(b) and 11(b) and Fig. 2(b) (pure tension), it is possible to measure the influence of the twist direction on the failure tensile strain. Inverse twisting induces a large influence on the CNT failure strain, reducing it to about one half (46.7%) of that for pure tension. For direct twisting, we obtained the same failure strain that we had for pure tension, with $\varepsilon_r = 0.275$ and $u_r = 11.3$ Å (see Fig. 2(a)–(b)). These results prove that, for the lower twist-to-tension ratio, $\Delta\phi/\Delta u = 0.349$ rad/Å (combination A), the chiral CNT twisted in the rolling direction of the hexagonal lattice breaks for the same axial displacement of a CNT under pure tension. For CNTs under low twist-to-tension rate (combination A), these results imply that direct twisting has no impact on the failure tensile strain while inverse twisting has a great influence on it. This conclusion is remarkable, if we consider that changing the direction of twisting makes the CNT break for half the pure tensile strain!

- For low twist-to-tension rate (combination A), the maximum energy at failure accumulated in the CNT under combined tension-direct twisting (1.5 eV atom – black curve in Fig. 10(a)) is much higher than that for pure tension (1.1 eV atom – Fig. 2(a)). Conversely, the maximum energy stored in the CNT under combined tension-inverse twisting (0.6 eV atom – gray curve in Figure 10(a)) is much lower than that for pure tension (1.1 eV atom – Fig. 2(a)).

- For high twist-to-tension rate (combination B), the maximum energies at failure accumulated in the CNTs under combined tension-direct twisting (0.67 eV atom – black curve in Fig. 10(b)) and combined tension-inverse twisting (0.50 eV atom – gray curve in Fig. 10(b)) are both lower than that for pure tension (1.1 eV atom – Fig. 2(a)).

- From the two previous statements, we conclude that the maximum energy stored in the (6,3) chiral CNT under combined tension-twist is generally lower that of a similar CTN under pure tension. The exception is the CNT under tension-direct twisting with low twist-to-tension rate (combination A). In this special case, the addition of small-to-moderate twist effects to the tensioned CNT increases the CNT energy beyond that of pure tension! As we will explain afterward, this

unexpected result is due to the stiffening effect arising from the direct twist action on the chiral CNT hexagonal lattice.

- Bearing in mind the stages I–IV defined for CNT under pure tension (Fig. 2(a and b)) and pure twisting (Fig. 6(a and b)), a similar classification can be applied to CNTs under combined tension-twisting. The characteristics of each stage exhibit monotonous behavior when sequentially considering systems undergoing pure tension, low twist-to-tension ratios, high twist-to-tension ratios and pure twisting.

- For a low twist-to-tension ratio (combination A), and before failure is achieved, both curves (gray and black) are very similar (nearly coincident) – see Fig. 10(b). This means that, for low twist-to-tension ratios, the stiffness of the chiral CNT is not influenced by the twist direction.

- For high twist-to-tension ratios (combination B), and before failure is achieved, the gray and black curves are very similar in stage I but become different in stage II, immediately after the occurrence of torsional buckling – see Fig. 11(b). This means that, for high twist-to-tension ratios, the direction of twisting (i) does not influence the linear behavior of the CNT (stage I), but (ii) affects its post-buckling stiffness (stages II and III).

- For low twist-to-tension ratios (combination A), the CNT under direct twisting completely breaks apart once rupture occurs, indicating global rupture (see the 2nd snapshot in Fig. 9(e_1)). This global rupture corresponds to the huge drop of force, seen in Fig. 10(b). On the contrary, the CNT under inverse twisting fails locally (see the 2nd snapshot in Fig. 9(c_2)) and experiences a sequential break of several bonds (see the 2nd snapshot in Fig. 9(d_2) and (e_2)). This local failure corresponds to the moderate drop of force, seen in Fig. 10(b), followed by a sequence of several smaller drops. From Fig. 10(a and b), we can see that failure arises much earlier for the CNT under inverse twisting ($\varepsilon_f = 0.144$, $u_f = 5.9$ Å, $\phi_f = 2.06$ rad) than for the case with direct twisting ($\varepsilon_f = 0.275$, $u_f = 11.28$ Å, $\phi_f = 3.94$ rad).

- For high twist-to-tension ratios (combination B), we can observe in Fig. 11(a and b) that the collapse is less sudden (force drops are smaller and more scattered) than the one observed in combination A conditions. Moreover, the failure occurs for slightly closer values between inverse twisting ($\varepsilon_f = 0.096$, $u_f = 3.95$ Å and $\phi_f = 2.39$ rad) and direct twisting $\varepsilon_f = 0.126$, $u_f = 5.17$ Å and $\phi_f = 3.13$ rad). In the pre-collapse stage, the grey curve (inverse twisting) displays very tiny drops, almost imperceptible in Fig. 11(a). These small drops are due to structural rearrangements that try to cope with the imposing twist. They do not correspond to C–C bond breaks as these imply larger energy drops. These structural rearrangements (Stone–Wales defects) occur when the cylindrical CNT structure is already ovalized, and reflect the wave-like radial distortions responsible for dispersing the local stresses arising from twisting. Such behavior is not seen in the black curve (direct twisting). In the post-collapse stage, and regardless of the twist direction, the energy variation shows small increases and drops, visible in Fig. 11(a), due to a sequence of bond rupture and formation of new bonds.

6. Conclusions

The twist-induced anisotropic behavior of (6,3) chiral CNT under combined tension-twisting is presented and discussed in this paper. CNT chirality triggers anisotropic responses that depend predominantly on the direction of twisting. The level of axial tension and the twist-induced anisotropy play a key role in the stiffness and strength of the chiral CNT. The most relevant conclusions are summarized next.

For pure tension, the load–displacement curve shows four stages (I – linear, II – non linear, III – linear, IV – post-failure). This four-stage behavior confirms the results previously obtained by other researchers. For pure twisting, the torque-twist curve also shows four stages (I – linear, II – initial post-buckling, III – linear hardening, IV – post-failure). After the initial linear path (stage I), the CNT buckles into a helix shape and its initial post-buckling stiffness (stage II) becomes almost null. For large twisting, the post-buckling stiffness increases in a slow rate (stage III) before failure occurs in stage IV. The post-failure strength displays some scatter (rises and drops) but the CNT ductility (deformation under large strain) is significant. The anisotropy induced by twisting the (6,3) chiral CNT was shown to be remarkable. The stiffness and strength of the chiral CNT was shown to be largely dependent on the direction of twisting. If the chiral CNT is twisted in the rolling direction of the hexagonal lattice (see Fig. 1), it is under direct twisting. On the contrary, if it is twisted "against the grain" it is under inverse twisting. The computed shear modulus for direct twisting was 25% higher than that for inverse twisting. Conversely, the buckling torque for inverse twisting was 40% higher than that for direct twisting. In the post-buckling regime, the torque evolves linearly with the twist and the CNT section becomes oval. The aspect ratio of the oval section for inverse twisting was 75% higher than that for direct twisting. Using classical mechanics, we explained that growing ovalization leads to torsional stiffness decrease. Thus, the post-buckling torsional stiffness for direct twisting was much higher than for inverse twisting. Despite the distinct behavior of the chiral CNT under direct and inverse twisting, the failure twist is only 5% apart. The computed shear strength for direct twisting is only 6% higher than that for inverse twisting. It should be emphasized that the twist-induced anisotropic behavior of the chiral CNT is much more noticeable when it concerns stiffness rather than strength.

The behavior of the (6,3) chiral CNT under combined tension-twisting is strongly dependent on (i) the twist direction and (ii) the twist-to-tension rate, thus evidencing its anisotropic nature. For the chiral CNT the under low twist-to-tension ratios, direct twisting has no impact on the failure strain (it equals the pure tensile strain) while inverse twisting has a great influence on it (it is half the pure tensile strain). For the chiral CNT under low twist-to-tension ratios, it is shown that the (6,3) accumulates much more energy when twisted directly than inversely. For direct twisting, the stored energy is even higher than that for pure tension. The addition of small-to-moderate direct twist to a tensioned CNT will increase its energy beyond

that of pure tension! This fact is due to the stiffening effect arising from the direct twist action on the chiral CNT hexagonal lattice. However, for high twist-to-tension ratios, the energy becomes lower than that of pure tension. For a low twist-to-tension ratio, both initial and post-buckling stiffnesses of the chiral CNT are not influenced by the twist direction. For high twist-to-tension ratios, the direction of twisting does not influence too much the initial stiffness of the CNT, but affects its post-buckling stiffness. The ductile (large deformation) behavior shown by the chiral CNT under pure twisting is lost when small-to-moderate tension is applied to the CNT. However, the post-failure mechanism of CNTs under combined tension-inverse twisting is more ductile (a smoother decrease of forces) while that of CNTs under combined tension-direct twisting is more brittle (a more sudden decrease of forces).

Acknowledgement

Appendix A. Supplementary data

Supplementary data associated with this article can be found, in the online version, at http://dx.doi.org/10.1016/j.mechmat.2012.11.004.

References

Agrawal, P.M., Sudalayandi, B.S., Raff, L.M., Komanduri, R., 2006. A comparison of different methods of Young's modulus determination for single-wall carbon nanotubes (SWCNT) using molecular dynamics (MD) simulations. Computational Materials Science 38, 271–281.

Agrawal, P.M., Sudalayandi, B.S., Raff, L.M., Komanduri, R., 2008. Molecular dynamics (MD) simulations of the dependence of C–C bond lengths and bond angles on the tensile strain in single-wall carbon nanotubes (SWCNT). Computational Materials Science 41, 450–456.

Chang, T., 2007. Torsional behavior of chiral single-walled carbon nanotubes is loading direction dependent. Applied Physical Letters 90, 201910.

Cooper, C.A., Young, R.J., 2000. Investigation into the deformation of carbon nanotubes and their composites through the use of Raman spectroscopy. Proceedings SPIE – Optical Devices and Diagnostics in Materials Science 4098, 172–181.

Dumitrica, T., Hua, M., Yakobson, B.I., 2006. Symmetry-, time-, and temperature-dependent strength of carbon nanotubes. Proceedings of the National Academy of Sciences 103, 6105.

Faria, B., Silvestre, N., Canongia Lopes, J.L., 2011. Interaction diagrams for carbon nanotubes under combined shortening-twisting. Composites Science and Technology 71, 1811–1818.

Faria, B., Silvestre, N., Canongia Lopes, J.N., in press. Tension-twisting dependent kinematics of chiral CNTs. Composites Science and Technology, http://dx.doi.org/10.1016/j.compscitech.2012.11.010.

Fennimore, A.M., Yuzvinsky, T.D., Han, W.Q., Fuhrer, M.S., Cumings, J., Zettl, A., 2003. Rotational actuators based on carbon nanotubes. Nature 424, 408–410.

Geng, J., Chang, T., 2006. Nonlinear stick-spiral model for predicting mechanical behavior of single-walled carbon nanotubes. Physical Reviews B 74, 245428.

Hall, A.R., An, L., Liu, J., Vicci, L., Falvo, M.R., Superfine, R., Washburn, S., 2006. Experimental measurement of single-wall carbon nanotube torsional properties. Physical Review Letters 96, 256102.

Jeng, Y.R., Tsai, P.C., Fang, T.H., 2004. Effects of temperature and vacancy defects on tensile deformation of single-walled carbon nanotubes. Journal of Physics and Chemistry of Solids 65, 1849–1856.

Jeong, B.W., Lim, J.K., Sinnott, S.B., 2007a. Tensile mechanical behaviour of hollow and filled carbon nanotubes under tension or combined tension-torsion. Applied Physical Letters 90, 023102.

Jeong, B.W., Lim, J.K., Sinnott, S.B., 2007b. Multiscale-failure criteria of carbon nanotube systems under biaxial tension-torsion. Nanotechnology 18, 485715.

Jeong, B.W., Lim, J.K., Sinnott, S.B., 2008. Tuning the torsional properties of carbon nanotube systems with axial prestress. Applied Physical Letters 92, 253114.

Khoei, A.R., Ban, E., Banihashemi, P., Abdolhosseini Qomi, M.J., 2011. Effects of temperature and torsion speed on torsional properties of single-walled carbon nanotubes. Materials Science and Engineering C 31, 452–457.

Leung, A.Y.T., Wu, Y.D., Zhong, W.F., 2006. Computation of Young's moduli for chiral single-walled carbon nanotubes. Applied Physical Letters 88, 251908.

Li, Y., 2010. Twist-enhanced stretchability of graphene nanoribbons: a molecular dynamics study. Journal of Physics D: Applied Physics 43, 495405.

Li, Z., Wang, S., Wang, Z., Zu, X., Gao, F., 2010. Mechanical behaviour of twinned SiC nanowires under combined tension-torsion and compression-torsion strain. Journal of Applied Physics 108, 013504.

Lu, J.P., 1997. Elastic properties of carbon nanotubes and nanoropes. Physical Review Letters 79, 1297.

Lu, W., Chou, T.W., Kim, B.S., 2011. Radial deformation and its related energy variations of single-walled carbon nanotubes. Physical Review B 83, 134113.

Marques, M.A.L., Troiani, H.E., Miki-Yoshida, M., Jose-Yacaman, M., Rubio, A., 2004. On the breaking of carbon nanotubes under tension. Nano Letters 4, 811–815.

Mylvaganam, K., Zhang, L.C., 2004. Important issues in a molecular dynamics simulation for characterizing the mechanical properties of carbon nanotubes. Carbon 42, 2025–2032.

Plimpton, S., 1995. Fast parallel algorithms for short-range molecular dynamics. Journal of Computational Physics 117, 1–19.

Silvestre, N., 2012. On the accuracy of shell models for torsional buckling of carbon nanotubes. European Journal of Mechanics A/Solids 32, 103–108.

Stuart, S.J., Tutein, A.B., Harrison, J.A., 2000. A reactive potential for hydrocarbons with intermolecular interactions. Journal of Chemical Physics 112, 6472–6486.

Sun, C., Liu, K., 2008. Combined torsional buckling of multi-walled carbon nanotubes coupling with axial loading and radial pressures. International Journal of Solids and Structures 45, 2128–2139.

Talukdar, K., Mitra, A.K., 2010. Influence of odd and even number of stone-wales defects on the fracture behaviour of an armchair single-walled carbon nanotube under axial and torsional strain. Molecular Simulation 36, 409–417.

Wang, C.M., Zhang, Y.Y., Xiang, Y., Reddy, J.N., 2010. Recent studies on buckling of carbon nanotubes. Applied Mechanics Reviews 63, 030804.

Williams, P.A., Papadakis, S.J., Patel, A.M., Falvo, M.R., Washburn, S., Superfine, R., 2002. Torsional response and stiffening of individual multiwalled carbon nanotubes. Physical Review Letters 89, 255502.